A Physics Based Multiscale Compact Model of *p-i-n* Avalanche Photodiodes

Sheikh Z. Ahmed , *Member, IEEE*, Samiran Ganguly , Yuan Yuan , *Member, IEEE*, Jiyuan Zheng , Yaohua Tan, Joe C. Campbell , and Avik W. Ghosh , *Senior Member, IEEE*

Abstract—III-V material based digital alloy Avalanche Photodiodes (APDs) have recently been found to exhibit low noise similar to Silicon APDs. The III-V materials can be chosen to operate at any wavelength in the infrared spectrum. In this work, we present a physics-based SPICE compatible compact model for APDs built from parameters extracted from an Environment-Dependent Tight Binding (EDTB) model calibrated to ab-initio Density Functional Theory (DFT) and Monte Carlo (MC) methods. Using this approach, we can accurately capture the physical characteristics of these APDs in integrated photonics circuit simulations.

Index Terms—SPICE, digital alloy, low noise.

I. INTRODUCTION

The rapid growth of Internet of Things (IoT) applications is resulting in the connection of more and more devices to the internet. There will be around 20.4 billion estimated IoT devices connected through machine-to-machine technology by the end of the year 2020 [1]. Furthermore, the advent of 5G communication technology will enable faster communication between wireless devices along with a reduction of over 90% in energy consumption compared to 4 G systems [2]. Thus, it is expected that 5G technology will enable an exponential growth in IoT devices and systems in the near future. This boom in telecom and data communication applications will drive the demand for more efficient and cheaper photonic integrated circuits (PICs) [3]. Only scalable, integrated photonic technologies can meet the huge demand coming from 5G and IoT technologies. Currently,

Manuscript received February 9, 2021; revised March 16, 2021; accepted March 17, 2021. Date of publication March 23, 2021; date of current version June 2, 2021. This work was supported in part by National Science Foundation under Grant NSF 1936016. (Corresponding author: Sheikh Ahmed.)

Sheikh Z. Ahmed, Samiran Ganguly, and Joe C. Campbell are with the Department of Electrical and Computer Engineering, University of Virginia, Charlottesville, VA 22904 USA (e-mail: sza9wz@virginia.edu; sganguly@virginia.edu; jcc7s@virginia.edu).

Yuan Yuan is with the Hewlett Packard Labs, Hewlett Packard Enterprise, Milpitas, CA 95035 USA (e-mail: yuan.yuan@hpe.com).

Jiyuan Zheng is with the Beijing National Research Center for Information Science and Technology, Tsinghua University, Beijing 100084, China (e-mail: zjy6@uchicago.edu).

Yaohua Tan is with the Synopsys Inc, Mountain View, CA 94043 USA (e-mail: yt5x@virginia.edu).

Avik W. Ghosh is with the Department of Electrical and Computer Engineering, University of Virginia, Charlottesville, VA 22904 USA, and also with the Department of Physics, University of Virginia, Charlottesville, VA 22904 USA (e-mail: ag7rq@virginia.edu).

Color versions of one or more figures in this article are available at https://doi.org/10.1109/JLT.2021.3068265.

Digital Object Identifier 10.1109/JLT.2021.3068265

there is a significant push to integrate III-V photonic devices onto the silicon platforms, that form the backbone of modern electronic devices. The prospect of coupling optical transmitters and receivers with the state-of-the-art complementary metal oxide semiconductor (CMOS) technology for compact IoT devices is highly enticing.

In the communication area, avalanche photodiodes (APDs) can achieve superior performance than conventional p-i-n photodiodes. The high internal gain of APDs, which arises from impact ionization, translates into greater receiver sensitivity and a dynamic operating range with accompanying increase in loss margins [4]–[7]. In addition to communications [8], APDs have been used in a wide range of applications including imaging, [9], [10] and single photon detection [11], [12]. The key challenge with APDs is the excess noise $F(M) = \langle m^2 \rangle/M^2$ due to the stochastic nature of the per primary-electron avalanche gain m of the impact ionization process [13]. The tightness of the carrier distribution is given by the McIntyre formula, whose popular form can be re-expressed as

$$F(M) - 1 = \frac{\sigma_m^2}{\langle m \rangle^2} = \frac{M - 1}{M} + k \frac{(M - 1)^2}{M}$$
 (1)

with the last quadratic term arising from secondary ionization processes by impact ionization of the minority carriers. The parameter k is the ratio of the hole ionization coefficient, β , to the electron ionization coefficient, α . Many techniques have been developed to reduce this excess noise [14]. All of these approaches focus on limiting the initiation of carrier multiplication to the carrier with the highest ionization rate.

Recently, some digital alloy III-V APDs, in essence short periodic superlattices with periodically stacked binary constituents, have experimentally demonstrated extremely low noise currents in the short infrared wave-length spectrum [15]–[17]. The underlying mechanism seems to correlate with the opening of minigaps in select subbands and the resulting change in available bandwidth from the bulk band edge to the minigap edge and effective mass of one of the carriers, although a thorough understanding of the physics is still evolving [15], [18], [19]. In this paper, we propose a simple circuit model of a *p-i-n* APD that is calibrated to both state-of-the art first-principles material studies as well as experimental devices. The model incorporates accurate material parameters like material effective mass and bandgap as well as fitting parameters for calibration. Our model enables accurate simulation of the circuit behavior

0733-8724 © 2021 IEEE. Personal use is permitted, but republication/redistribution requires IEEE permission. See https://www.ieee.org/publications/rights/index.html for more information.

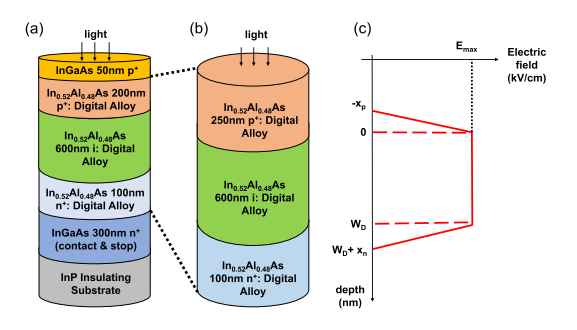


Fig. 1. (a) Schematic diagram of experimental InAlAs digital alloy APD (b) Schematic diagram of simplified device considered for SPICE model (c) Electric field profile of the simulated *p-i-n* APD.

of state-of-the-art digital alloy APDs in PICs, all the way from first-principles studies of underlying materials to circuits.

We study the material bandstructure of these alloys using an environment-dependent tight binding model (EDTB), which is calibrated to state-of-the-art DFT bandstructure and wavefunctions computed using hybrid functionals (HSE06) [20]. The bandstructure of some of the digital alloys with low noise characteristics show small gaps called 'minigaps' in their valence bands, that reduce hole ionization, generating a small ratio k in Eq. (1). The transport properties of these digital alloy APDs are calculated using full-band Monte Carlo simulations, which show a good match with experimental results. In order to study their performance in circuits, a SPICE compatible model is required. Circuit models for both p-i-n APDs and separate absorption, charge, and multiplication (SACM) APDs have been reported [21]-[23]. Previously reported p-i-n APD circuit models [21] use bulk material parameters that fail to capture the quantum effects, such as minigaps, seen in these short-period superlattices. Thus, it is necessary to develop a simple physics-based circuit model that can include the interesting physical properties observed in today's newer materials.

The various tools and models used for the simulation of APDs in this paper are described in the following sections. In Section II of this paper, we describe the bandstructure model, the full-band Monte Carlo model and then the proposed circuit model. In Section III we show simulations performed using this circuit model along with calibrations to experimental data.

II. MODEL

In this work we consider short period III-V digital alloys for our simulation. In particular, we will study the characteristics of a digital alloy InAlAs *p-i-n* APD. Fig. 1(a) shows a schematic cross-section of the device [15]. For SPICE modeling, we consider a simplified structure shown in Fig. 1(b). The typical electric field profile of this device is given in Fig. 1(c). We can see that the highest electric field is in the intrinsic region where the avalanche multiplication occurs. For the simulations in this paper, the electric field is considered to be uniform in this region.

The properties of III-V digital alloy APDs differ largely from their bulk counterparts due to the band unfolding imposed by the overall superlattice periodicity. It is therefore imperative to develop a solid modeling framework that accounts for the band

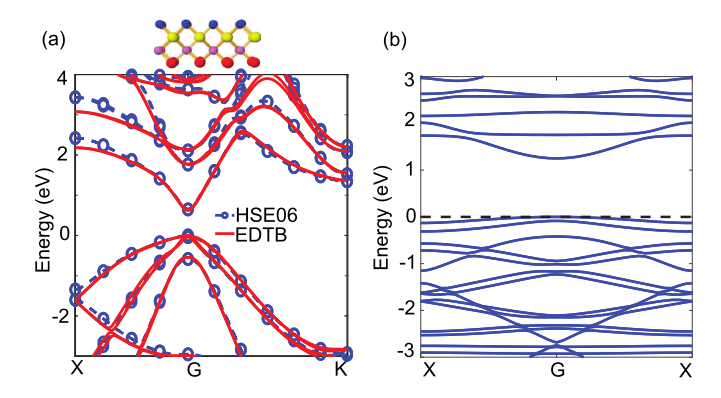


Fig. 2. (a) Comparison of our environment-dependent tight binding model to density functional theory simulations and previous tight binding results for a InGaAsSb alloy [28]. (b) Bandstructure of 6-monolayer digital alloy InAlAs considered in this paper.

modification, device geometry and various scattering processes in our SPICE model. We use state-of-the-art band structure and transport models calibrated to first-principles based results and experiments, which makes our tools very reliable for simulating existing and emerging APD structures. The tools are described in the following subsections.

A. Bandstructure Model

As a first step, the detailed band structure of the material is calculated using the environment dependent tight binding (EDTB) model. The accuracy of the EDTB is underscored by the need for precise material parameters used in the circuit simulations. Conventional tight binding is benchmarked to bulk bandstructures and not readily transferrable to surfaces and interfaces where the environment impacts the chemistry substantially. Readjusting the parameters is not straightforward, as these methods work directly with the eigenvalues, i.e., E-k relationships, and do not work with the full eigenvectors, especially their radial parts that determine bonding and tunneling (only the angular parts of the orbitals are used to enforce the overall group theoretical symmetry). Our past attempt at due diligence on radial eigenvectors was to use Extended Hückel theory [24], [25] which employed explicit Wannier basis sets constructed from non-orthogonal atomic orbitals that were fitted to arrive at the bulk Hamiltonian. Since the basis sets were fitted rather than the energies, the latter were transferrable to other environments that simply required recomputing the overlap matrix elements. In contrast, the EDTB model works within conventional orthogonal Wannier like basis sets, and is not only calibrated to DFT band structure but also wavefunctions that are based on experiments and first-principles calculations [20], [26]. For the DFT bandstructure and wavefunctions calculations we employ the HSE06 hybrid functional approximation which predicts material band structure accurately [27]. The accuracy of our EDTB model for a InGaAsSb alloy is described in Fig. 2(a) [28]. It shows that the bandstructure of InGaAsSb calculated with the EDTB model replicates the bandstructure obtained using DFT very precisely. Fig. 2(b) shows the EDTB band structure of a 6-monolayer

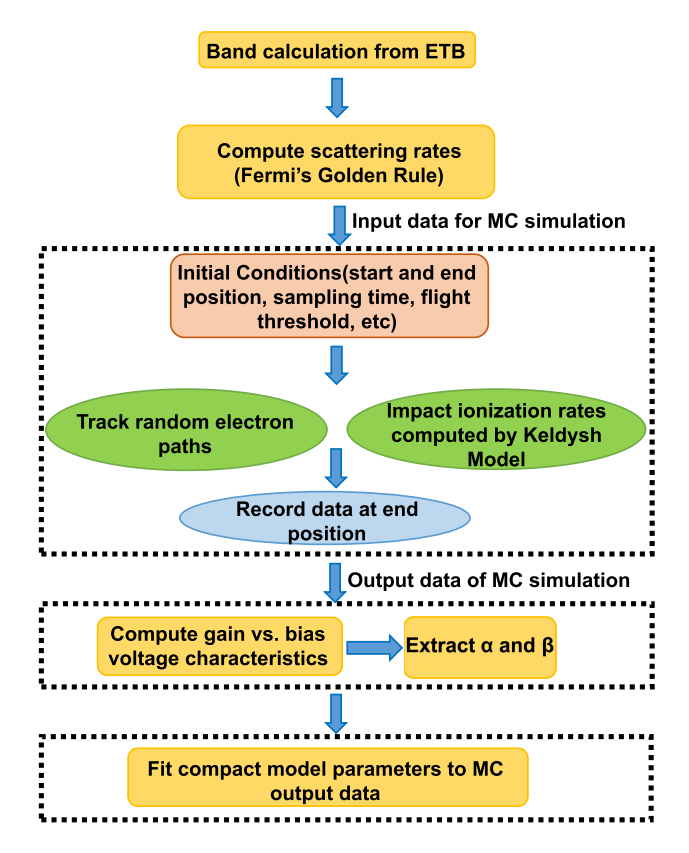


Fig. 3. Flowchart of Monte Carlo simulation process.

InAlAs digital alloy used in this simulation. The resulting band structure is fed into a full band Monte Carlo simulator.

B. Monte Carlo Simulation

The Monte Carlo simulation tracks the transport behavior of injected electrons. The flowchart of the method used for extracting device parameters is shown in Fig. 3. Initially, the scattering rates are calculated using Fermi's Golden Rule, incorporating the full bandstructure obtained from the EDTB model. The Monte Carlo simulation results used in this paper consider deformational potential scattering. The deformational scattering rate $P_{\nu\nu',n}^{def}(\mathbf{k},\Omega_{\mathbf{k}\pm\mathbf{q}})$ from a point \mathbf{k} in band ν to a region $\Omega_{\mathbf{k}'}$ in band ν' centered around \mathbf{k}' is expressed as [19], [29]

$$P_{\nu\nu,'n}^{def}(\mathbf{k}, \Omega_{\mathbf{k}\pm\mathbf{q}}) = \frac{\pi}{\rho\omega_{nq}} |\Delta^{n}(\nu,'\mathbf{k}, \mathbf{q}, \nu)|^{2} |I(\nu, \nu'; \mathbf{k}, \mathbf{k}\pm\mathbf{q})|^{2}$$

$$D_{\nu'}(E,'\Omega_{\mathbf{k}'}\left(N_{nq} + \frac{1}{2} \mp \frac{1}{2}\right)$$
(2)

where, ρ represents the lattice density, \mathbf{q} is the phonon wave vector of mode n and the deformation potential is $\Delta^n(\nu, '\mathbf{k}, \mathbf{q}, \nu)$.

The path of a single electron through the multiplication region is then tracked under the effects of electric field and random scattering events. The impact ionization rates used in the simulation are computed using the Keldysh model [30], described below. The impact ionization rate using this model is expressed by [19], [29]

$$P_{m'}(\mathbf{k}, \mathbf{k}') = S(E - E_{th})^{\gamma} \tag{3}$$

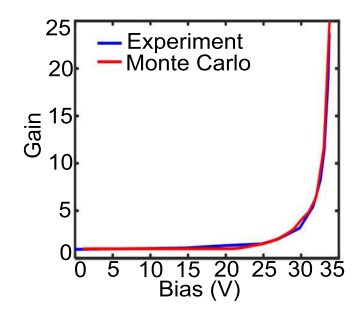


Fig. 4. Gain vs. reverse bias voltage characteristics for the InAlAs APD.

where, E_{th} is the threshold energy, S is the softness parameter and γ is an approaching index. We can approximate the threshold energy by $E_{TH} = E_G(2\mu^{-1}+1)/(\mu^{-1}+1)$ where E_G is the material bandgap and μ^{-1} is the ratio of the electron effective mass to the hole effective mass. This expression assumes a two-band model, i.e., a conduction band and a valence band. For equal conduction and valence band mass, E_{TH} is equal to 1.5 times the bandgap E_G . The expression is widely used to approximate the threshold energy in APDs. These parameters were adjusted by fitting the gain curves and excess noise of the Monte Carlo simulation results with experimental results. The simulation is repeated for multiple electrons and carrier transport properties are computed by averaging over the many trajectories [31]. From the ensemble Monte Carlo simulation, we obtain the gain versus bias voltage characteristics, as shown in Fig. 4 for an InAlAs APD.

The electron and hole ionization coefficients, α and β respectively, can be calculated using the following equations:

$$\alpha(\mathcal{E}) = \frac{1}{W_D} \left[\frac{M_n(V) - 1}{M_n(V) - M_p(V)} \right] ln \left[\frac{M_n(V)}{M_p(V)} \right]$$
(4)

$$\beta(\mathcal{E}) = \frac{1}{W_D} \left[\frac{M_p(V) - 1}{M_p(V) - M_n(V)} \right] ln \left[\frac{M_p(V)}{M_n(V)} \right]$$
 (5)

where, $M_n(V)$ and $M_p(V)$ represent the gain of the electrons and holes respectively, $\mathcal{E}=V/W_D$ is the electric field and W_D is the width of the multiplication region. This ratio is an important metric for determining the excess noise factor F(M) of APDs. By varying parameters like temperature and repeating the MC simulations we can extract the relationship of the ionization coefficients with these parameters. Then the extracted ionization coefficients, their ratio and the gain can be re-expressed in terms of simpler empirical functions that are then used for the compact model:

$$k = c_1 e^{c_2 T} \tag{6}$$

$$\alpha(T,\mathcal{E}) = c_3 exp \left[-c_4 T - \left(\frac{c_5}{\mathcal{E}}\right)^n \right] \tag{7}$$

$$M = \frac{k-1}{k - exp\left[\alpha(1-k)W_D\right]} \tag{8}$$

where $M=M_n$ for pure electron injection and M_p for pure hole injection. In other words, the ionization coefficients are reduced to six material-dependent constants c_{1-5} and n that are

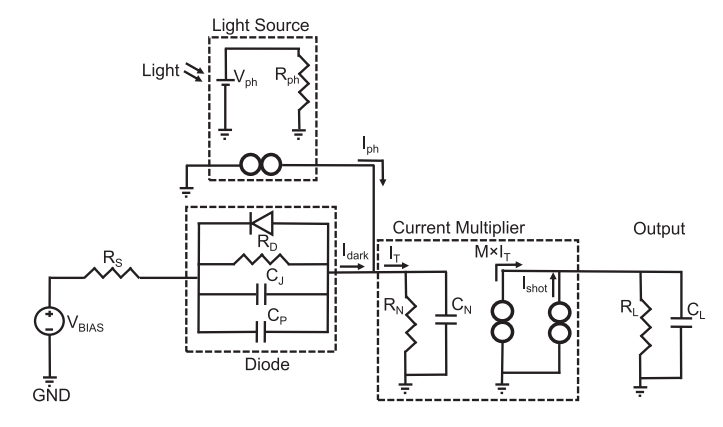


Fig. 5. Schematic diagram of avalanche photodiode model and testbench used in the SPICE simulations.

extracted from numerical data on the gain curve, such as from experiments or the ensemble Monte Carlo approach described earlier. The fitted parameters are used to calculate the voltage dependent impact ionization gain in the circuit model.

C. Circuit Model

In this section we describe the SPICE compatible physics-based circuit model. The circuit layout of the compact model is displayed in Fig. 5. The unit cell consists of a simple diode coupled to a light source unit and a current multiplier unit to model the APD characteristics. For our model, we consider a dark current that consists of two components: the reverse bias saturation current and the tunneling current. The dominating current at low reverse bias is the current through the resistor R_D . The value of R_D can be calibrated from experimental I-V characteristics or theoretically computed by diode reverse bias saturation current using material parameters. The tunneling current flowing through the diode symbol, I_{TUN} , considering a triangular barrier, is calculated using the Fowler-Nordheim equation.

$$I_{TUN} = \frac{\sqrt{2m^*}q^3 \mathcal{E} V_{bias} A}{4\pi^2 \hbar^2 E_G^{1/2}} exp \left[-\frac{\Theta \sqrt{2m^*} E_G^{3/2}}{q \hbar \mathcal{E}} \right]$$
(9)

The parameters m^* , V_{bias} , A and E_G represent the tunneling effective mass, the bias voltage across the p-i-n structure, cross-sectional area and the bandgap, respectively. The fitting parameter Θ is used to account for the difference in barrier shape with that of an experimental device. For a triangular barrier we can consider $\Theta=4/3$. Another current component, I_L , is used to model other various leakage currents through the diode like Shockley-Read-Hall generation and trap-assisted tunneling

$$I_L = I_{L0} e^{\zeta V_{bias}} \tag{10}$$

For calibration with InAlAs APD experimental data and simulations in this paper we consider I_{L0} and ζ as fitting parameters. The total dark current, I_{dark} , is then given by

$$I_{dark} = \frac{V_{bias}}{R_D} + I_{TUN} + I_L \tag{11}$$

The photocurrent I_{ph} is modeled as a voltage controlled current source. The photon source is modeled as a voltage source, V_{ph} , connected to a large resistor, R_{ph} . The source input power P_{IN} , which is proportional to V_{ph} , is determined by

$$P_{IN} = V_{ph} \times 1amp \tag{12}$$

$$I_{ph} = q\eta \frac{P_{IN}(1-R)}{hc/\lambda} \left[1 - e^{-a_p W_p} \right]$$
 (13)

Eq. (13) gives the photocurrent, I_{ph} . In the equation R is the reflectivity of the absorption region, a_p is the absorption coefficient, W_P is the p-region width and λ gives the wavelength of the input light source. η represents the internal quantum efficiency. For a given material, the theoretical value of η can be numerically calculated using [32]

$$\eta(\lambda, T) = \frac{E_g \int_{E_G}^{\infty} D(E) f(E) dE}{\int_0^{\infty} ED(E) f(E) dE}$$
(14)

where, D(E) and f(E) are the photon density of states and occupancy (given by Bose-Einstein statistics) functions.

The reason a voltage source is preferred for the photon source is that internally SPICE models use all nodal equations as I=GV type matrices when the simulations are set up, i.e. the voltages V are independent variables, and the currents I are dependent. Therefore, any current-controlled voltage source or current-controlled current source element needs to be converted to an equivalent voltage-controlled current source or voltage-controlled voltage source element using Thevenin equivalent. This matters only for large simulations or to guard against convergence issues, particularly if the resistance, R, is very small since this makes the conductance G matrix singular. In this case since R is very large this is not a consideration.

The current multiplier models the avalanche multiplication of the APD. The multiplier takes the sum of the unmultiplied dark and photo current given by (15) as input and multiplies that by the gain M, which is a function of the reverse bias voltage given by (8). The output current of the APD is finally obtained by (16)

$$I_T = I_{dark} + I_{ph} (15)$$

$$I_{out} = M \times I_T \tag{16}$$

The noise sources of the APDs must also be included in the model to accurately model their behavior in circuit applications. In the model, noise currents are modeled as separate current sources. In this paper, we can consider only the dominant shot noise of the APDs. For a given bandwidth Δf , the noise variance of the shot noise is given by

$$\langle i_{shot}^2 \rangle = 2q(I_{dark} + I_{ph})\langle M^2 \rangle F(M)\Delta f$$
 (17)

It is possible to extract the APD bandwidth, Δf , from MC simulation. The average impulse function for a large number of short input photon pulses, shaped like Gaussian pulses, can be extracted from MC simulation [33]. The decaying tail of the the impulse function can be fitted by the function $h(t) = 2\pi\eta M q \Delta f exp(-2\pi\Delta ft)u(t)$, where u(t) is a unit step function, having a value of one for all positive t and zero for the rest. Here, Δf is the frequency at which APD's gain drops to 0.707 of

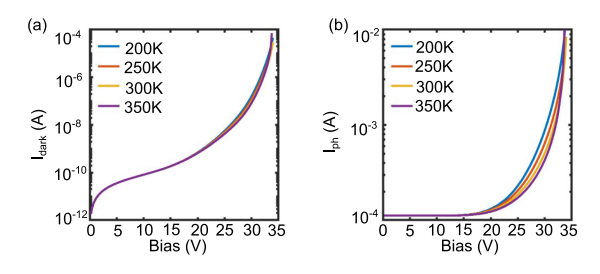


Fig. 6. (a) Dark current vs. reverse bias voltage characteristics (b) Photo current vs. reverse bias voltage characteristics. Both plots are given as a function of temperature.

its maximum value, which is the 3 dB bandwidth. It is important to point out that the bandwidth of a circuit, where APD is a component, can be dominated by other circuit elements besides the APD. However, those extrinsic effects can be captured by our compact circuit model where the APD enters as a component block.

For transient calculations, capacitances are added in parallel to the diode. C_J represents the intrinsic capacitance of the device and C_P is the parasitic capacitance. A resistor R_S is added in series to the bias voltage source to model the contact resistances. A small resistor and capacitor, R_N and C_N , are used at the output of the diode to help with convergence in SPICE. R_L and C_L are the load resistor and capacitor used to extract the output. The values used in this paper are listed in Table I and are obtained from a previous publication [34]. These can be computed from MC simulations.

In summary, given any digital alloy combination our compact model can take material parameters like bandgap and effective mass as input and outputs relevant metrics of APD circuit simulation like dark current, gain, quantum efficiency and noise current. The dark current is obtained from eq. (11), gain from eq. (8), quantum efficiency from eq. (14) and APD excess noise current from eq. (17). These metrics are calculated based on calibrations to MC simulation or experimental results.

III. RESULTS AND DISCUSSION

The temperature dependent reverse bias I-V characteristics are shown in Fig. 6(a). At low bias the current is dominated by the diffusion current density which is a constant in the device. The large current at high bias is attributed to the increasing tunneling current and increasing gain of the device. At high bias, the current reduces with increased temperature due to increased phonon scattering occurring in the device, captured through our scattering rates that enter the Monte Carlo simulations and are eventually lumped into the c_{1-5} and n parameters. Fig. 6(b) shows the photo-current vs. reverse bias voltage for different temperatures. It exhibits a similar trend at high bias like the dark current due to the increasing gain and phonon scattering. For this plot we considered $P_{IN}=1$ mW.

In Fig. 7(a) the simulated reverse bias dark current characteristics of the InAlAs digital alloy APD using the calibrated compact model are plotted and compared to the experimental measurements [15]. The calibrated parameters are given in

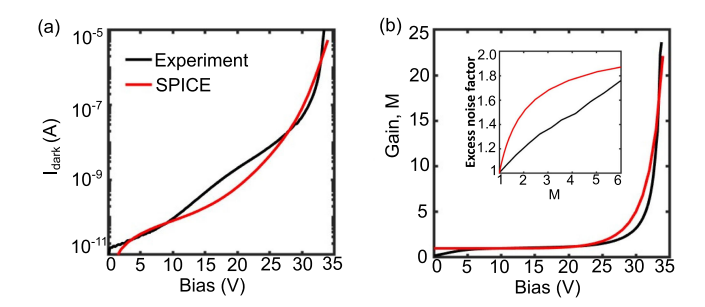


Fig. 7. (a) Calibration of the simulated dark current characteristics using SPICE model of a 6-monolayer InAlAs digital alloy APD (b) Calibrated of the simulated gain vs. bias characteristics of this APD. Inset-Excess noise factor vs. gain of computed using McIntyre's Formula compared to the experimental results.

TABLE I
TABLE OF MAJOR PARAMETER VALUES USED IN SPICE MODEL

Parameter	Value
η	40%
c_1	0.012
R	0.01
c_2	$0.0147~K^{-1}$
m^*	$0.08m_0$
c_3	$2.2 \times 10^7 \ cm^{-1}$
E_G	$1.25 \ eV$
c_4	$0.004~K^{-1}$
n	0.9
c_5	$3.5 \times 10^6 \ Vcm^{-1}$
a_p	$1.57 \times 10^4 \ Vcm^{-1}$
$\frac{a_p}{A}$	$31.4 \ nm^2$
λ	$1.08~\mu m$
R_D	$1.5 \times 10^{11} \Omega$
I_{L0}	$5.3 \times 10^{-13} A$
$\frac{\zeta}{\zeta}$	$0.3414\ V^{-1}$
k	0.01
Θ	0.8
T	300 K
W_P	250 nm
C_J	5.77 pF
R_L	0.1 Ω
$\overline{C_L}$	1 <i>pF</i>

Table I. The simulated values agree well at low and high bias. There is a small discrepancy in the middle region that is due to the use of the approximate equations used in calculating some of the parameters which results in overestimation of the scattering processes involved. Additionally, some discrepancy is due to the simplification of the structure considered in the simulation. This is primarily to allow for faster convergence of the SPICE model. Fig. 7(b) shows the simulated gain versus bias characteristics compared to the experimental data. The values are in good agreement with each other. To calculate the excess noise factor versus gain characteristics we use the standard McIntyre's formula [13]. The comparison between the calculated and experimental F versus M is shown in the inset of Fig. 7(b). We observe that McIntyre's formula overestimates the excess noise at low gain values compared to experiments. The mismatch can be attributed to simplifications, like ignoring the 'dead-space' effect. For APDs with large multiplication regions, the dead-space effect can be ignored and good agreement can be achieved using McIntyre's formula.

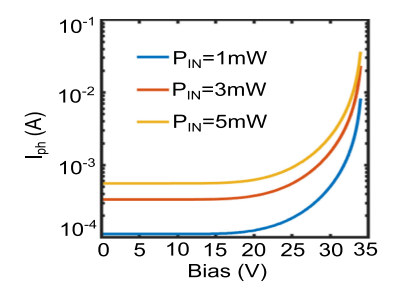


Fig. 8. Photocurrent vs. reverse bias voltage characteristics as a function of input power.

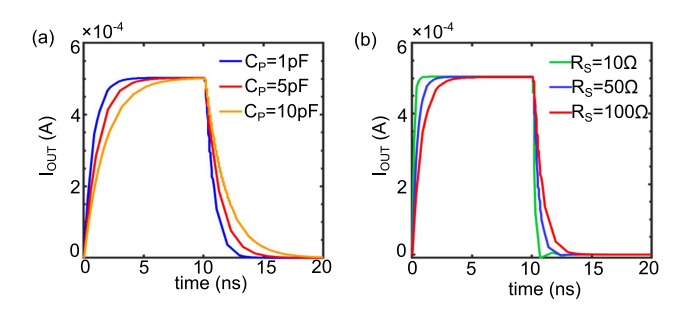


Fig. 9. (a) Transient response of output current with varying parasitic capacitance, C_P (b) Transient response of output current as a function of contact resistance, R_S .

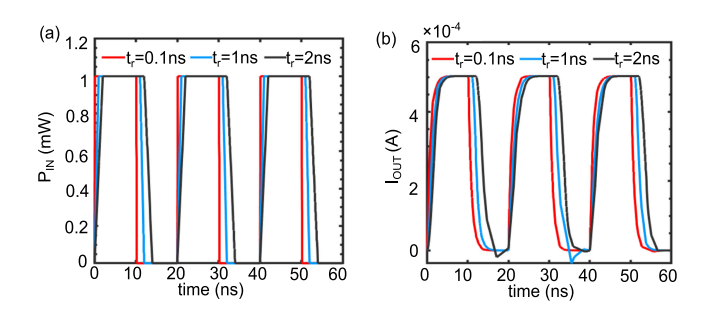


Fig. 10. (a) Input power (light source) vs. time for different rise and fall times (b) output current vs. time for the different rise and fall times.

We plot the output I-V characteristics for different input powers in Fig. 8. A higher input power of the light source results in more electron-hole pair generation in the absorption region. This increases the current at low bias. At very high bias, the APD reaches the avalanche breakdown region where the output current is not affected much by the input power magnitude due to the high carrier generation by the impact ionization process.

The transient characteristics of the InAlAs digital alloy APD considered in this compact model are shown in Figs. 9 and 10. The bias voltage used is 30 V. The transient response of the output current for different parasitic capacitance is simulated in Fig. 9(a). We can see that the parasitic capacitance present in the APD can significantly affect its responsiveness to the input light. A larger capacitance results in longer rise and fall times. In a receiver this will translate to lower detection speed and will affect the overall speed of an integrated photonic device. The effect of different contact resistances on the output transient

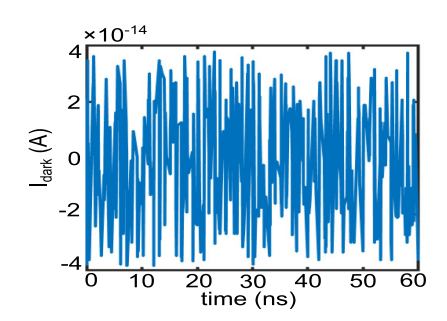


Fig. 11. Simulated shot noise of the InAlAs APD.

response is shown in Fig. 9(b). Increased contact resistance also leads to higher rise and fall times. However, the effect of R_S is not as significant as the parasitic capacitances.

Fig. 10 shows input and output characteristics of the APD for different rise and fall times. It is seen that a longer rise/fall time results in slower discharge at the end of each input cycle and can also result in overshoots while discharging. This shows that switching pattern of the light source can also affect the refresh rate of the APD.

One of the crucial elements of APD performance is the excess noise that is generated due to the random nature of the impact ionization process. Any noise can significantly degrade the photon detection ability of these photodetectors. Thus, it is necessary to include the noise in the circuit model in order to accurately model PICs. This noise is reduced by allowing impact ionization to be initiated by carrier injection of the carrier with the highest ionization coefficient. This essentially translates to a lower value of the ionization coefficient ratio k.

Fig. 11 shows the dominant shot noise in the dark current simulated using the SPICE model. The noise current is added as a separate current source in the circuit. We consider $\Delta f=1~{\rm Hz}$ since it is generally application dependent. Many methods are used to reduce the shot noise in the APDs. In the InAlAs digital alloy APD the noise is minimized due to the presence of "minigaps" in the valence band which prevents holes from ionizing and thus suppress F(M) [15]. Although in this treatment we only consider shot noise as the dominant source in digital APDs, we can in principle include other types of noise relevant for different geometries as added current sources.

Despite the model being developed for *p-i-n* APDs, it can be modified to simulate other structures such as Separate Absorption Charge Multiplication (SACM) APDs as well. The potential profile of the SACM APDs can be obtained using added electrostatic solvers, which can then be used as input to the MC model. The fitting parameters of the compact model, described in section II-B and II-C, can be adjusted to match the results of the MC simulations. The compact model might require some additional resistance and capacitance elements to account for the behavior of the absorption and charge layers of the SACM structure. This will attach additional components to the unmultiplied dark current. The equation for gain given in Section II-C will still be valid, with slight alterations to the fitting parameters for calibration, as the physics of the multiplication

region remains unchanged. Also, empirical equations might be required to capture the voltage dependencies of some of the parameters used in the unmultiplied photocurrent.

IV. CONCLUSION

In this paper, we report an elementary physics-based compact model of APDs. This model captures the essential device physics calculated by first-principles methods and simulates their effect on circuit behavior. The compact model ultimately treats the APD as a black box that can be included in a modular fashion into bigger photonic integrated circuits, with its input being material and geometric parameters and output being relevant performance metrics such as excess noise, gain, dark current and quantum efficiency. In particular, we simulate the behavior of a new class of digital alloy APDs which exhibit low excess noise at very high bias, which makes them highly suitable for a wide range of applications.

ACKNOWLEDGMENT

The authors would like to thank for fruitful discussions with Seth Banks and Andreas Beling.

REFERENCES

- S. Li, L. Da Xu, and S. Zhao, "5G internet of things: A survey," J. Ind. Inf. Integr., vol. 10, pp. 1–9, 2018.
- [2] M. Z. Chowdhury, M. K. Hasan, M. Shahjalal, E. B. Shin, and Y. M. Jang, "Opportunities of optical spectrum for future wireless communications," in *Proc. Int. Conf. Artif. Intell. Inf. Commun.*, Feb. 2019, pp. 004–007.
- [3] A. Y. Liu and J. Bowers, "Photonic integration with epitaxial III-V on silicon," *IEEE J. Sel. Topics Quantum Electron.*, vol. 24, no. 6, pp. 1–12, Nov. 2018.
- [4] S. D. Personick, "Receiver design for digital fiber optic communication systems, Parts I and II," *Bell Syst. Tech. J.*, vol. 52, no. 6, pp. 843–886, 1073
- [5] R. Smith and S. Personick, "Receiver design for optical fiber communication systems," *Semiconductor Devices for Optical Communication*. Berlin, Germany: Springer, 1980, pp. 89–160.
- [6] S. Forrest, "Sensitivity of avalanche photodetector receivers for high-bitrate long-wavelength optical communication systems," in *Semiconductors* and *Semimetals*, Elsevier, vol. 22, 1985, pp. 329–387.
- [7] B. Kasper and J. Campbell, "Multigigabit-per-second avalanche photodiode lightwave receivers," *J. Lightw. Technol.*, vol. 5, no. 10, pp. 1351–1364, 1987.
- [8] J. C. Campbell, "Advances in photodetectors," Optical Fiber Telecommunications VA. Elsevier, 2008, pp. 221–268.
- [9] N. Bertone and W. Clark, "Avalanche photodiode arrays provide versatility in ultrasensitive applications," *Laser Focus World*, vol. 43, no. 9, 2007.
- [10] P. Mitra et al., "Adaptive focal plane array (AFPA) technologies for integrated infrared microsystems," *Intell. Integr. Microsyst.*, vol. 6232. *Int. Soc. Opt. Photon.*, 2006, Art no. 62320G.
- [11] A. Tosi, N. Calandri, M. Sanzaro, and F. Acerbi, "Low-noise, low-jitter, high detection efficiency InGaAs/InP single-photon avalanche diode," *IEEE J. Sel. Topics Quantum Electron.*, vol. 20, no. 6, pp. 192–197, Nov./Dec. 2014.
- [12] X. Jiang et al., "Inp-based single-photon detectors and geiger-mode apd arrays for quantum communications applications," *IEEE J. Sel. Topics Quantum Electron.*, vol. 21, no. 3, pp. 5–16, May/Jun. 2015.
- [13] R. McIntyre, "Multiplication noise in uniform avalanche diodes," *IEEE Trans. Electron Devices*, no. 1, pp. 164–168, Jan. 1966.
- [14] J. C. Campbell, "Recent advances in avalanche photodiodes," *J. Lightw. Technol.*, vol. 34, no. 2, pp. 278–285, Jan. 2016.
- [15] J. Zheng et al., "Digital alloy inalas avalanche photodiodes," J. Lightw. Technol., vol. 36, no. 17, pp. 3580–3585, 2018.
- [16] Y. Yuan et al., "Comparison of different period digital alloy Al_{0.7} InAsSb avalanche photodiodes," J. Lightw. Technol., vol. 37, no. 14, pp. 3647–3654, Jul. 2019.

- [17] X. Yi et al., "Extremely low excess noise and high sensitivity ALAs_{0.56}Sb_{0.44} avalanche photodiodes," *Nature Photon.*, vol. 13, no. 10, pp. 683–686, Jul. 2019. [Online]. Available: http://eprints.whiterose.ac. uk/148333/
- [18] J. Zheng, Y. Tan, Y. Yuan, A. W. Ghosh, and J. C. Campbell, "Strain effect on band structure of InAlAs digital alloy," *J. Appl. Phys.*, vol. 125, no. 8, 2019, Art no. 0 82514.
- [19] J. Zheng et al., "Full band monte carlo simulation of AlInAsSb digital alloys," InfoMat, vol. 2, no. 6, pp. 1236–1240, 2020.
- [20] Y. Tan, M. Povolotskyi, T. Kubis, T. B. Boykin, and G. Klimeck, "Transferable tight-binding model for strained group IV and III-V materials and heterostructures," *Phys. Rev. B*, vol. 94, Jul. 2016, Art no. 0 45311.
- [21] W. Chen and S. Liu, "PIN avalanche photodiodes model for circuit simulation," *IEEE J. Quantum Electron.*, vol. 32, no. 12, pp. 2105–2111, Dec. 1996.
- [22] J.-J. Jou, C.-K. Liu, C.-M. Hsiao, H.-H. Lin, and H.-C. Lee, "Time-delay circuit model of high-speed pin photodiodes," *IEEE Photon. Technol. Lett.*, vol. 14, no. 4, pp. 525–527, Apr. 2002.
- [23] A. Banoushi, M. Kardan, and M. A. Naeini, "A circuit model simulation for separate absorption, grading, charge, and multiplication avalanche photodiodes," *Solid-State Electron.*, vol. 49, no. 6, pp. 871–877, 2005.
- [24] D. Kienle, J. I. Cerda, and A. W. Ghosh, "Extended hückel theory for band structure, chemistry, and transport. I. carbon nanotubes," *J. Appl. Phys.*, vol. 100, no. 4, 2006, Art no. 0 43714.
- [25] D. Kienle, K. H. Bevan, G.-C. Liang, L. Siddiqui, J. I. Cerda, and A. W. Ghosh, "Extended hückel theory for band structure, chemistry, and transport. II. Silicon," *J. Appl. Phys.*, vol. 100, no. 4, 2006, Art no. 0 43715.
- [26] Y. P. Tan, M. Povolotskyi, T. Kubis, T. B. Boykin, and G. Klimeck, "Tight-binding analysis of Si and GaAs ultrathin bodies with subatomic wavefunction resolution," *Phys. Rev. B*, vol. 92, no. 8, 2015, Art no. 0 85301.
- [27] J. Heyd, G. E. Scuseria, and M. Ernzerhof, "Hybrid functionals based on a screened coulomb potential," *J. Chem. Phys.*, vol. 118, no. 18, pp. 8207–8215, 2003.
- [28] S. Z. Ahmed, Y. Tan, D. S. Truesdell, B. H. Calhoun, and A. W. Ghosh, "Modeling tunnel field effect transistors-from interface chemistry to nonidealities to circuit level performance," *J. Appl. Phys.*, vol. 124, no. 15, 2018, Art. no. 154503.
- [29] J. Zheng et al., "Simulations for InAlAs digital alloy avalanche photodiodes," Appl. Phys. Lett., vol. 115, no. 17, 2019, Art. no. 171106.
- [30] G. Dunn, G. Rees, J. David, S. Plimmer, and D. Herbert, "Monte carlo simulation of impact ionization and current multiplication in short gaas diodes," *Semicond. Sci. Technol.*, vol. 12, no. 1, p. 111, 1997.
- [31] J. Zheng et al., "A pmt-like high gain avalanche photodiode based on GaN/AlN periodically stacked structure," Appl. Phys. Lett., vol. 109, no. 24, 2016, Art no. 241105.
- [32] S. Ganguly, M.-H. Jang, Y. Tan, S.-S. Yoo, M. C. Gupta, and A. W. Ghosh, "A multiscale materials-to-systems modeling of polycrystalline pbse photodetectors," *J. Appl. Phys.*, vol. 126, no. 14, 2019, Art. no. 143103.
- [33] A. S. Huntington, *InGaAs Avalanche Photodiodes for Ranging and Lidar*. Woodhead Publishing, 2020.
- [34] Y. Yuan et al., "Temperature dependence of the ionization coefficients of InAlAs and AlGaAs digital alloys," *Photon. Res.*, vol. 6, no. 8, pp. 794–799, 2018.

Sheikh Z. Ahmed (Member, IEEE) received the B.Sc. degree from BRAC University, Dhaka, Bangladesh, in 2014. He is currently working toward the Ph.D. degree with the University of Virginia, Charlottesville, VA, USA. His research interests include the computational study of nanoelectronic and photonic devices, quantum transport, and compact modeling. He is also a Member of the APS and SPIE.

Samiran Ganguly received the Ph.D. degree from Purdue University, West Lafayette, IN, USA, under the guidance of Prof. Supriyo Datta. He is currently a Research Scientist with the University of Virginia, Charlottesville, VA, USA. He co-founded and co-developed the Modular Approach to Spintronics, the largest open source collection of circuit modules for modeling complex structures and devices using emerging materials technology and phenomena. His recent research has focused on exploration of neuromorphic computing using this approach for applications in signal processing for edge devices. He is also working on developing theory and modeling of emerging infrared detectors and their close integration with neuromorphic backends for building smart cameras with spatio-temporal machine intelligence and autonomous sensory-motor devices.

Yuan Yuan (Member, IEEE) received the B.S. degree in electrical engineering from the Nanjing University of Aeronautics and Astronautics, Nanjing, China, in 2016 and the Ph.D. degree in electrical engineering from the University of Virginia, Charlottesville, VA, USA, in 2019. He is currently a Research Scientist with Hewlett Packard Labs of Hewlett Packard Enterprise. His research interests include avalanche photodiodes, single photon counting, and III-V and silicon photonics. He is a Member of OSA.

Jiyuan Zheng received the Ph.D. degree in electronic engineering from Tsinghua University, Beijing, China, in 2017. From 2017 to 2019, he was a Postdoc with the University of Virginia, Charlottesville, VA, USA, where he worked on digital alloy avalanche photodiode. From 2019 to 2020, he joined The University of Chicago, Chicago, IL, USA, as a Postdoc to work on single-photon avalanche photodiode. In 2020, he moved to Beijing National Research Center for Information and Science Technology as an Assistant Research Scientist. His research interests include single-photon detection, neuromorphic photonics computing, and optoelectronics devices.

Yaohua Tan received the Ph.D. degree from Purdue University, West Lafayette, IN, USA, in 2015. From 2016 to 2018, he was with University of Virginia, Charlottesville, VA, USA, as a Postdoc Research Scientist. Since 2018, he has been with Synopsys. Inc, CA, USA. His research interests include the modeling of quantum transport and device reliability physics, parameter extraction from first principle and quantum phenomena in low dimensional materials.

Joe C. Campbell received the B.S. degree in physics from the University of Texas at Austin, Austin, TX, USA, in 1969, and the M.S. and Ph.D. degrees in physics from the University of Illinois at Urbana-Champaign, Champaign, IL, USA, in 1971 and 1973, respectively. From 1974 to 1976, he was employed by Texas Instruments, where he worked on integrated optics. In 1976, he joined the staff of AT&T Bell Laboratories, Holmdel, NJ, USA. He was with Crawford Hill Laboratory, where he worked on a variety of optoelectronic devices including semiconductor lasers, optical modulators, waveguide switches, photonic integrated circuits, and photodetectors with emphasis on high-speed avalanche photodiodes for high-bit-rate lightwave systems. In January 1989, he joined the faculty of the University of Texas at Austin as a Professor of electrical and computer engineering and the Cockrell Family Regents Chair of engineering. In January of 2006, he became a Member of the faculty with the University of Virginia, Charlottesville, VA, USA, as the Lucian Carr, III Chair of electrical engineering and applied science. He has coauthored ten book chapters, 450 articles for refereed technical journals, and more than 400 conference presentations. His research focuses on the optoelectronic components that are used to generate, modulate, and detect the optical signals. He is currently actively involved in single-photon-counting avalanche photodiodes, Si-based optoelectronics, high-speed, low-noise avalanche photodiodes, ultraviolet photodetectors, and quantum-dot IR imaging. He is a Member of the National Academy of Engineering.

Avik Ghosh (Senior Member, IEEE) received the B.S. and M.S. degrees in physics from the Indian Institute of Technology, Kanpur, India, and the Ph.D. degree in physics from The Ohio State University, Columbus, OH, USA. He is currently a Professor with the Departmentt of Electrical and Computer Engineering and Departmentt of Physics (by courtesy). He was a Research Scientist with the Department of Electrical and Computer Engineering, Purdue University, West Lafayette, IN, USA, and moved to UVA in 2005. He founded the Virginia NanO Computing Lab. His group develops theory, modeling and simulation tools for nonequilibrium electron flow in nanomaterials. He has more than 100 refereed papers and book chapters, and is the author of two upcoming books in nano-electronics and low power devices, specializing in materials to systems modeling including 2D materials, thin films for photodetectors, molecular electronics, nanomagnetic materials, and neuromorphic computing. He is the UVA Site Director of the NSF Industry University Cooperative Research Center on Multifunctional Integrated Systems Technology, and the Director of a DARPA Team on skyrmion based topological excitations in electronics. He is a Fellow of the Institute of Physics, Editorial Board Member of IEEE-Nano and Proceedings of the Royal Society A. He was the recipient of the IBM Faculty Award, the NSF CAREER Award, the Best Paper Award from the Army Research Office, and the UVA's All University Teaching Award. His group's collaborative research with Columbia University on observing negative index behavior in graphene was voted by Physics World Editors as one of the top-10 physics breakthroughs of 2016.